Three-Dimensional Wind-Driven Coastal Circulation past a Headland

CLINTON D. WINANT

Integrative Oceanography Division, Scripps Institution of Oceanography, University of California, San Diego, La Jolla, California

(Manuscript received 27 September 2004, in final form 19 October 2005)

ABSTRACT

Local velocities and the trajectories of fluid parcels forced by wind blowing over a continental shelf, in the vicinity of a headland, are described with a linear, steady, three-dimensional barotropic model. The dynamical balance that governs the transport is similar to the wind-driven general circulation, because the varying bottom depth acts in the same way as meridional variation in the rotation rate. Far from the headland the circulation is independent of alongshore position, and the transport is parallel to the coast. The alongshore pressure gradient is a significant term in the alongshore momentum balance. Near the headland, the amplitude of the circulation, including the vertical motion, is larger on the upwave side (the side toward which a Kelvin wave would travel) than on the downwave side. On the upwave side, the flow adjusts to the presence of the headland over a distance of order $\delta_E B^*$, where δ_E is the ratio of the Ekman depth to the maximum shelf depth and B^* is the width of the shelf. Fluid parcels that upwell on the upwave side are drawn from deeper depths than parcels that upwell at other alongshore locations. On the downwave side the flow adjusts over a relatively long distance, of order $\delta_E^{-1} B^*$.

1. Introduction

In *The Oceans,* Sverdrup et al. (1942) note that upwelling along the coasts of California and Peru has variable intensity, with lowest temperatures regularly occurring in certain localities. In their early description of the California Current system, Reid et al. (1958) further note that "this effect (upwelling) seems to be intensified south of capes and points which extend out into streams." Many published images of sea surface temperature along upwelling shores document alongshore inhomogeneity in the temperature field. Frequently the coldest temperatures occur on the upwave side (the side toward which a Kelvin wave would travel) of coastal promontories. Determining why colder temperatures are found on one side of a promontory is complicated by the fact that surface wind stress has been shown to vary considerably in the vicinity of a headland (Winant et al. 1988; Winant and Dorman 1997). The observed enhanced upwelling could be the result of larger wind stress, or be caused by the influence of the topography on the flow. Here a simple linear model of the steady, three-dimensional, upwelling circulation on a well-mixed, idealized continental shelf is used to describe the effect of a headland on the circulation driven by spatially constant wind.

One way to sort out the effect of variable topography from variable wind stress is to construct models that include alongshore variations in the topography but maintain the wind stress spatially constant. Gan and Allen (2002) compute numerically the three-dimensional circulation driven by spatially uniform wind stress along the continental shelf and show that the circulation varies in the alongshore direction, with colder surface temperatures south of all capes. The much simpler model described here also predicts asymmetric response, with much larger horizontal and vertical velocities on the upwave side of the headland. When the wind is upwelling favorable, fluid parcel trajectories that come close to the upwave side are drawn from deeper depths than other parcels, consistent with the observations.

The steady-state response of continental shelf waters to wind forcing has already received considerable attention in the literature. Pedlosky (1974a,b) describes the steady wind-driven circulation near the boundaries of a closed stratified basin. The closed nature of the basins used in both analyses has the advantage of avoiding ambiguities associated with prescribing boundary

Corresponding author address: Clinton Winant, Integrative Oceanography Division, Scripps Institution of Oceanography, University of California, San Diego, 9500 Gilman Dr., La Jolla, CA 92093.
E-mail: cdw@coast.ucsd.edu

conditions on open boundaries. When the walls of the basin are vertical (Pedlosky 1974b), the circulation is shown to depend primarily on the components of the wind stress with the largest alongshore scales. The depth structure of the upwelling is also dependent on the longshore scale. When the basin has a sloping bottom bounded by two vertical walls (Pedlosky 1974a), there is a "topographic boundary layer" seaward of the shallow wall, in which the pressure anomaly is governed by a parabolic equation. In this region solutions can only be found downwave from alongshore locations where boundary conditions are applied.

Csanady (1978) considers a similar problem, in which the coastal area is unbounded in the offshore direction and open along the coast. The fluid density is taken to be constant, and this and other simplifications lead to an equation governing the sea level that is also parabolic. The solution obtained for a patch of wind predicts sea level rising in the downwind direction under the patch (the pressure gradient force opposes the wind stress) and decreasing farther downwave. The solution continues to evolve in the longshore direction and never becomes two-dimensional, because of the infinite cross-shore extent of the continental shelf. Pringle (2002) has extended the Csanady (1978) model to show that an alongshore wind drives enhanced onshelf transport in a coastal ocean if the shelf widens downwind. When the wind is upwelling favorable, the increased transport is in the bottom boundary layer and brings cold, nutrient-rich water close to the coast.

Because the equations that govern the pressure in the Pedlosky (1974a) and Csanady (1978) models are parabolic, boundary conditions on both up- and downwave alongshore locations, as arise in the case of a headland, cannot be satisfied. Pringle (2002) recognized this limitation and noted that boundary layers that are dynamically equivalent to the Stommel (1948) solution for the Gulf Stream appear under such conditions. Here, the restrictions imposed by a parabolic equation are avoided by adapting the model proposed by Winant (2004) to describe the wind-driven flow over the continental shelf, in a geometry similar to the one used by Pedlosky (1974a). The model is kept conceptually as simple as possible, to focus attention on the pressure field and on the alongshore variability induced by a headland. The assumption of steady state implies that the described circulation is that which persists after transients have died out. An important feature of this model is the retention of the term that represents bottom friction in the cross-shelf direction. With cross-shelf friction, the governing equation is elliptic, and the dynamics become similar to the wind-driven general circulation (Stommel 1948; Welander 1976), because the varying bottom depth acts in the same way as the meridional variation in the rotation rate.

2. The model

Consider an elongated channel on the f plane. The x axis is parallel to the coast and the y axis extends offshore. In the Northern Hemisphere, the positive x direction is downwave (corresponding to the direction of Kelvin wave propagation), and the negative direction is upwave. Here, z is measured positive up from the undisturbed surface. The constant-density fluid is driven by a wind stress vector $\boldsymbol{\tau}^*(x, y)$ (dimensional variables are starred). An upwelling-favorable wind stress is negative. In addition, $\mathbf{u}^*$ is the horizontal velocity vector and w^* is the vertical velocity; η^* is the position of the surface relative to $z = 0$. At the surface the vertical velocity gradient is set to $\boldsymbol{\tau}^*/\rho K$, where K represents the constant vertical eddy viscosity, and $w^* = 0$. The three components of velocity are set to zero at the bottom. Lateral mixing is ignored because the ratio $K_h H^{*2}/KB^{*2}$ (K_h represents the horizontal eddy viscosity, H^* is the maximum depth, and B^* is the shelf width) is assumed to be small. As a consequence, only the transport streamfunction or its normal derivative need to be specified on the sides of the channel. The model equations are developed in detail by Winant (2004). Briefly, the vertical profile of the horizontal velocity and the horizontal transport are related to the wind stress and the pressure gradient through the Ekman solutions. When combined with the continuity equation, these relations can be manipulated to give an expression for the transport streamfunction that depends only on the wind stress, as is shown in the appendix. The relative importance of friction to rotation, measured by $\delta_E = \sqrt{2K/fH^{*2}}$, the ratio of the Ekman depth to H^*, is the only parameter to emerge from this derivation. If the basin depth is taken to be 150 m, and the Ekman depth is taken as 15 m, then $\delta_E = 0.1$, a value used for the calculations described here.

Away from the headland, between $y^* = 0$ and $y^* = B^*$, the depth $h^*(x, y)$ varies from some small value to H^*. To facilitate the numerical calculations the depth at the coast ($y^* = 0$) is $0.025H^*$, rather than zero. The width of the continental shelf, B^*, is taken to be the characteristic horizontal length scale. Farther offshore the depth remains equal to H^*. The nondimensional width of the basin is Y, where $Y \geq 2$. The up- and downwave ends of the channel are considered to be open, with the boundary condition that the transport is parallel to the coast, or $\psi_x = 0$. However, to fix the offshore boundary condition, the channel is considered closed at some large distance upwave from the region of immediate interest, where the wind forcing is envi-

sioned to go to zero, as is the case in real upwelling regions. This means that the transport streamfunction at the offshore wall, located at $y = Y$, has the same value as at the coast, or that the net transport across any section perpendicular to the coast is zero. This condition is similar to the boundary condition applied by Pedlosky (1974a).

The headland, centered at $x = 0$, is modeled as a narrow promontory within the otherwise uniform basin. At $x = 0$ the nondimensional depth is given by

$$\begin{aligned} h(0, y) &= 0.025 \quad \text{for} \quad 0 \le y \le 0.5 \\ &= 0.025 + 1.95(y - 0.5) \quad \text{for} \quad 0.5 \le y \le 1 \\ &= 1 \quad \text{for} \quad 1 \le y \le 2. \end{aligned} \tag{1}$$

Over the top of the headland, between $y = 0$ and $y = 0.5$, the water depth is the same as the depth at the coast, again to facilitate the numerical solution. The promontory merges smoothly into the general bathymetry over an alongshore distance x_h on either side of $x = 0$:

$$h(x, y) = h(x_h, y) + [h(0, y) - h(x_h, y)]\frac{x_h - x}{x_h} \quad \text{for} \quad |x| < x_h, \tag{2}$$

where $h(x_h, y)$ represents the bathymetry everywhere except near the headland. For the simulation described here, $x_h = 0.04$.

3. Wind-driven flow by a headland

If a steady upwelling-favorable wind ($\tau_s^x = -1$) blows parallel to shore ($\tau_s^y = 0$) with constant amplitude, the streamfunction Eq. (A21) simplifies to

$$(A\psi_x)_x + (A\psi_y)_y + B_x\psi_y - B_y\psi_x = -C_y\tau_s^x - (D\tau_s^x)_x, \tag{3}$$

where A [Eq. (A18)], a function of δ_E and h, is a parameter that represents friction. In the limit of high rotation, it corresponds to the coefficient of friction in the Stommel (1948) model. In addition, B [Eq. (A18)] represents rotation. In the limit of high rotation, B_y corresponds to $\partial f/\partial y$ in the Stommel (1948) model. When $\tau_s^x = 1$ over the whole field, Eq. (3) is the same as the equation solved by Winant (2004) for a closed basin driven by uniform wind. In that case, if the basin is long enough, the solution consists of three parts. Near midbasin the streamfunction depends only on y and the flow is two-dimensional. Near each end, boundary layers accommodate the two-dimensional solution to the boundary condition that ψ has a constant value along all boundaries. The structure and the dynamics in these turning areas depend on the sign of the bottom slope and on δ_E. The boundary layer ahead of an observer looking downwave is narrow and governed by dynamics that are similar to the western boundary currents in models of the wind-driven ocean circulation. This is called a Stommel layer. Behind the observer, the boundary layer is broad and the dynamical balance is consistent with the Sverdrup balance modified by friction, and with the arrested topographic wave solution proposed by Csanady (1978). The structure of the flow driven by constant wind around a headland, the problem considered here, can be described in terms of these flow structures.

a. The far field

Far from the headland, the streamfunction is expected to not depend on x. This region is similar to the two-dimensional region in the middle of the wind-driven basin in the Winant (2004) solution. The components of the pressure gradient [Eqs. (A16) and (A17)] are then

$$\eta_x = A\psi_y^\infty + C\tau_s^x \quad \text{and} \tag{4}$$

$$\eta_y = -B\psi_y^\infty + D\tau_s^x = -\frac{P_i}{P_r}\eta_x - \frac{Q_i\tau_s^x}{P_r}, \tag{5}$$

where Ps and Q [Eqs. (A10) and (A11)] are functions of δ_E and h, and ψ^∞ is the far-field streamfunction. Since ψ^∞ and h are independent of x in the far field, Eq. (5) shows that η_y does not depend on x. Then η must be the sum of separate function of x and y, and η_x cannot depend on y. With the condition of no net alongshore transport through any section parallel to the coast, $\langle U\rangle = \langle\psi_y^\infty\rangle = 0$ (where $\langle\rangle$ denotes the average value across the width of the basin), the alongshore pressure gradient can be evaluated from Eq. (4) divided by A, and averaged across the width of the basin:

$$\eta_x = \frac{\langle C\tau_s^x/A\rangle}{\langle 1/A\rangle} = -\frac{\langle (Q_r + P_iQ_i/P_r)\tau_s^x\rangle}{\langle P_r + P_i^2/P_r\rangle}. \tag{6}$$

In Fig. 1, η_x and $\delta_E\eta_y$ driven by an upwelling wind ($\tau_s^x = -1$) are illustrated for different values of Y, for $0 \le y \le 1.3$. Here, η_y remains constant beyond the shelf ($y > 1$), where the depth is constant. For upwelling, the alongshore pressure gradient is negative: sea level rises downwind, in the sense to drive a flow upwind. In the limit as Y becomes very large, $\eta_x \to \tau_s^x$, so the alongshore pressure gradient persists independent of the width of the basin, so long as the condition of no net transport across a section is imposed. The major difference between the flow described here and published analyses (Janowitz and Pietrafessa 1980; Lopez and Clarke 1989; Allen et al. 1995; Allen and Newberger 1996; Tilburg 2003) of two-dimensional wind-driven

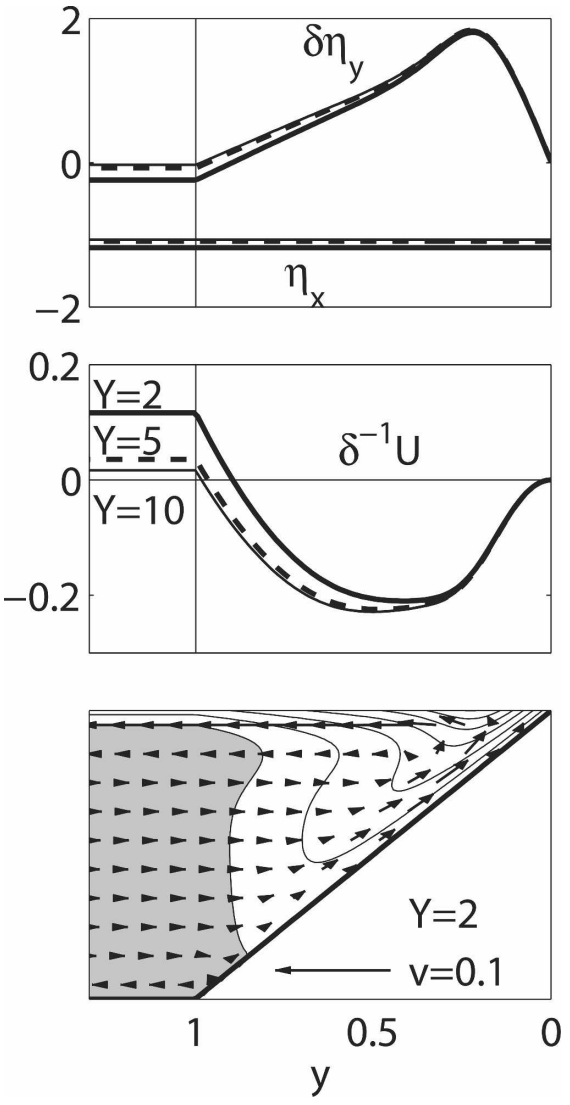

FIG. 1. (top) Pressure gradients, (middle) transport, and (bottom) local velocities in the far field ($|x| \gg 1$), for $\delta^{-1} = 10$. The wind stress is negative (upwelling favorable). The cross-shelf dimension increases toward the left (looking toward $+x$). Solutions are illustrated up to $y = 1.3$. They remain constant for larger values of y. Pressure gradients and transport are illustrated for three different basin widths: $Y = 2$ (thick solid line), $Y = 5$ (dashed line), and $Y = 10$ (thin solid line). Here, η_x is independent of y. For an upwelling alongshore wind, the alongshore transport $U = -\psi_y^\infty$ is negative (downwind) over most of the shelf. In the bottom panel, the alongshore velocity is represented by contours and shading, for $Y = 2$ only. The light areas represent negative (downwind) flow. The cross-shore and vertical velocities are represented by the arrows.

coastal circulation is the nonzero alongshore pressure gradient required in this model to satisfy the no net alongshore transport requirement. On the shelf η_y is positive, corresponding to the sea level increasing with distance from the coast, for an upwelling wind.

The transport streamfunction can be evaluated from Eq. (4):

$$\psi_y^\infty = \frac{1}{A}(\eta_x - C\tau_s^x). \tag{7}$$

The alongshore transport, $U = -\psi_y^\infty$, is illustrated in Fig. 1. The solutions for different values of Y represent a broad downwind transport over the shelf and an upwind transport offshore. There is no cross-shelf transport ($\psi_x = 0$). The amplitude of $\delta_E^{-1}U$ depends only weakly on δ_E. This implies that the dimensional vertically integrated alongshore transport U^* scales as $\tau_0\delta_E H^{*2}/(\rho K)$. The alongshore component of current therefore scales as $\tau_0\delta_E H^*/(\rho K) = 2\tau_0/(\rho\delta_E H^* f)$. Friction drives the transport to zero at the coast and the transport reaches maximum amplitude (a coastal jet) on the shelf, at a location that depends only weakly on δ_E. Over the shelf the transport depends only weakly on Y. For this reason, the remaining calculations are made with $Y = 2$. Off the shelf, the transport has to balance the downwind transport on the shelf. Since the offshore transport is distributed between $1 \le y \le Y$, it diminishes with increasing Y. Given η, the local horizontal velocities are calculated from Eq. (A6), and the vertical velocity is integrated down from the surface, using the continuity equation. Local velocities, computed for $Y = 2$, are illustrated in the bottom panel of Fig. 1. The alongshore flow is downwind over most of the shelf and everywhere near the surface. The return flow, required to keep the net transport zero, forms an undercurrent, off the shelf and beneath the surface. Near shore the alongshore flow is weak because of friction. The amplitude of the alongshore flow first increases with distance from shore, reaching a maximum in a coastal jet at midshelf, and then decreasing with further distance offshore. The lateral circulation consists of two superimposed gyres. The main gyre, located in the upper part of the water column, rotates in the sense expected from Ekman dynamics: the surface flow is to the right of the wind and, for $\tau_s^x = -1$, there is upwelling near the coast. The compensating onshore flow is above the bottom boundary layer. A second, weak gyre is located near the bottom off the shelf and is driven by veering in the bottom Ekman layer.

b. Flow near the headland

Based on the discussion in Winant (2004), the flow immediately upwave of the headland is expected to adjust in a relatively narrow Stommel layer, while downwave the flow tends back to the far-field solution over a relatively long distance. The two adjustment regions are matched at $x = 0$. To illustrate these features, the

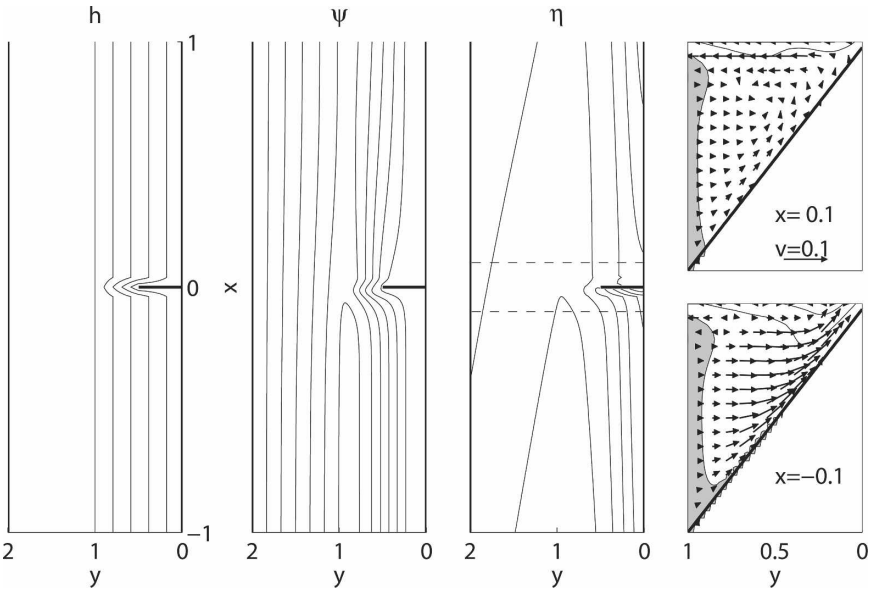

FIG. 2. The circulation driven by upwelling-favorable wind stress around a headland. The three contour maps on the left represent the depth, the transport streamfunction, and the sea level, respectively. The domain shown (from $x = 1$ to $x = -1$) is a subset of the domain in which the fields have been computed. The depth ranges from 0.025 at the coast and over the headland to 1 for $y > 1$. The streamfunction is everywhere positive or zero. The contour interval is 0.002. Sea level (negative everywhere) is shown in the third frame. It is a minimum at the coast and rises offshore and downwind. Sections of the local velocities over the shelf ($0 \leq y \leq 1$), on either side of the headland, are illustrated in the right-most frame. Unshaded areas represent downwind flow.

streamfunction has been computed numerically in a domain that extends between $x = \pm 8$ in the alongshore direction and between $y = 0$ and $y = 2$. Equation (A21) is solved using the multigrid iteration scheme proposed by Adams (1989), subject to the boundary conditions that $\psi = 0$ on $y = 0$ and $y = 2$, and $\psi_x = 0$ on $x = \pm 8$. The bathymetry between $x = \pm 1$ is illustrated in the left-hand panel of Fig. 2. The streamfunction is illustrated in the second panel of Fig. 2. Far from the headland, in both the up- and downwave directions, the numerical solution tends toward the two-dimensional solution described above. The streamlines turn from the coast near $x = 0$. On the upwave ($x < 0$) side the adjustment takes place within a Stommel layer, over a distance of order δ_E. On the downwave side the adjustment is spread over a distance of order δ_E^{-1}.

The sea level, computed from Eq. (A15), is illustrated in the third panel of Fig. 2. For upwelling, the topography of the sea surface in the far field is as described in the previous section: sea level rises downwind, and increases from the coast to the edge of the shelf, in approximate geostrophic balance with the downwind transport over the shelf. Close to the headland, the sea level response is asymmetric, depending on alongshore position. Upwave from the headland, it reaches a minimum value at the upwave corner, and sea level gradients are larger than anywhere else in the field. The low pressure, where the flow is ageostrophic, makes the transport turn around the corner. On the downwave side, the pressure is relatively higher than on the other side, and changes are distributed over a larger alongshore extent.

Local velocities are evaluated using Eq. (A6), and the vertical velocity is integrated down from the surface. Both up- and downwave from the headland the velocities tend to the two-dimensional solution, illustrated in Fig. 1. Sections of the velocity at an alongshore distance of ± 0.1 from the coast are illustrated in the right-most panels of Fig. 2. The upwave–downwave asymmetry is pronounced. The alongshore velocity is qualitatively similar to the pattern for the two-dimensional region, although the amplitude of the velocity is reduced. The lateral circulation is both qualitatively and quantitatively different than that in the two-dimensional region. On the downwave side ($x > 0$), the cross-shelf and vertical velocities are weak, except for the very near surface offshore flow that is directly driven by the wind. On the upwave side ($x < 0$), where the turning caused by the headland occurs over a fairly narrow distance, the cross-shelf and vertical velocities are large

compared with other locations, and upwelling velocities penetrate to greater depth than anywhere else.

Fluid parcel trajectories identify the location from where upwelled water is drawn. The trajectories of four parcels that end up near the surface ($z = -0.05$), at a fixed distance from the coast ($y = 0.75$), on the upwave side of the headland are illustrated in Fig. 3. Two of the parcels released downwave of the obstacle ($x = 0.5$ and $x = 1.2$) and the parcel released upwave ($x = -0.3$) are very similar: they are all drawn from similar depth (z between -0.3 and -0.5), and the alongshore extent of the trajectories is comparable. Fluid parcels released farther up- or downwave follow nearly identical trajectories. The parcel that comes closest to the upwave side of the headland differs from the others in two important ways: it is drawn from deeper water ($z = -0.78$) and it travels over a relatively short alongshore distance. After release, the parcel moves slowly downwind with relatively little vertical or cross-shelf motion until it passes over the obstacle. Then it is entrained into the relatively fast upwelling flow shown in the lower right-hand panel of Fig. 3. These trajectories illustrate the point that the headland effectively forces a deeper vertical exchange on the upwave side. They also illustrate how promontories increase the dispersion between fluid parcels.

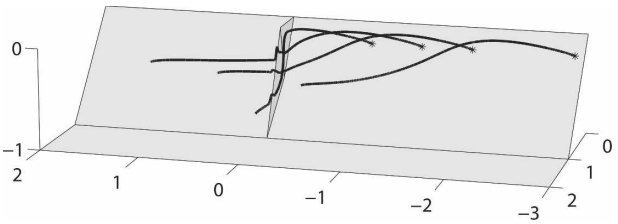

FIG. 3. Trajectories of four fluid parcels released at various locations for upwelling-favorable wind. The final position is marked by the asterisk, and the shallow ($z = -0.05$) final depth is the same for each parcel. The trajectories of parcels released some distance up- or downstream of the headland are similar and are all drawn from between $z = -0.33$ and -0.475. The parcel released just upstream of the obstacle, at $x = 0.5$, is drawn from deeper depth: $z = -0.78$.

4. Discussion

Gan and Allen (2002) describe with a numerical model the three-dimensional time-dependent circulation that develops along the California coast, north of Point Reyes, driven by spatially uniform, time-dependent, wind stress. Their analysis is focused on the poleward flow that has been observed to develop when the wind stress relaxes to zero after a period of sustained upwelling. Before this happens, when the wind stress is both spatially and temporally uniform, the computed flow exhibits considerable alongshore variability related to the alongshore changes in the topography. In particular they find that the coldest water is found to the south (upwave side) of capes, as the model presented here would suggest. The sea surface elevation field computed in the numerical model reaches its lowest values south of capes. In this region, the negative pressure gradient (for upwelling-favorable winds) is accompanied by geostrophically balanced onshore flow throughout the water column and by positive vertical velocities on the inner shelf. In the model presented here the sea surface is minimum just upwave of the cape (Fig. 2). There, the cross-shelf flow is onshore, and the vertical velocity is positive at all depths. The parcel trajectories illustrated in Fig. 3 show that water from the deepest depth (coldest water) surfaces to the south of the cape. Thus, the kinematic descriptions from both models are reasonably consistent, but the underlying dynamics are different.

Gan and Allen (2002) interpret the flow calculated with the numerical model as follows. Alongshore velocities are shown to increase in magnitude as the current flows around the obstacle. The lower pressure at the coast occurs in order to maintain a geostrophic balance for the increased alongshore velocity and decreases even further because of the gradient wind effect (the pressure gradient required to turn a flow), an advective process that is not considered in the model presented here. On the south side the onshore flow, accompanied by positive vertical velocities, is in geostrophic balance with the alongshore pressure gradient. On the north side, the positive pressure gradient balances both the offshore flow and nonlinear advective terms.

There are important dynamical differences between the very simple model presented here and the more sophisticated numerical simulation. Perhaps the most significant of these concerns the detailed structure of the elevation field in the vicinity of the cape. In this model, the area just south of the cape is a relatively narrow Stommel layer where the pressure field changes rapidly. In the Gan and Allen (2002) study, the elevation changes most rapidly on the north side of the cape, where the pressure gradients are largest. There is no evidence of a structure similar to the Stommel layer in the numerical simulations, and there are at least two possible reasons for this. The first has to do with the neglect of nonlinear advective terms that are identified as significant factors in the numerical solution. The second is related to the absence in this model of any realistic density structure that is bound to modify the importance of friction in a more complete model.

Given these differences, it is reasonable to ask to what extent the linear model that is presented here

represents the essential dynamics that govern the real flow. This model does not include unsteady or stratified conditions, and advection has been neglected. Even with these restrictions, the model does produce a realistic description of the upwelling circulation, with offshore flow confined within a surface Ekman layer balanced either by subsurface onshore flow when the circulation is two-dimensional or by divergence in the alongshore flow. This model also produces a realistic description of the cross-shelf structure of the alongshore flow, as illustrated in Fig. 1, including a maximum (coastal jet) some distance from the coast. It describes a pattern of sea level variability (lower sea level at the coast with upwelling) that is consistent with observations. It produces quantitative estimates of the alongshore velocities that are consistent with observations. Last, it provides an explanation for the observation that colder water is found on the upwave side of coastal promontories. While beyond the scope of this work, it would be interesting to understand which processes included in the numerical model are responsible for the differences noted above. One way to do this would be to simulate the flow in the simple geometry used in this model with a numerical simulation of increasing complexity to determine how each of the neglected processes modifies the circulation.

Beyond the very early descriptive reports quoted at the beginning of this paper, more recent observation confirm that the coldest upwelled waters are found downwave of capes (Huyer and Kosro 1987). However, the very simplicity of this model, and the omission of processes that are shown by more thorough numerical studies to be important, makes any further quantitative comparison pointless. Complexities in a real upwelling environment associated with large spatial inhomogeneities in the wind field make more detailed comparisons even more futile.

Acknowledgments. Thanks are given to Jamie Pringle who made several useful suggestions on an early version of this paper. Suggestions and comments from two anonymous reviewers helped to clarify the paper. The work described here was supported by a 2003 UC MEXUS-Conacyt grant and by NSF Grant OCE-0425029.

APPENDIX

Model Equations

Nondimensional (unstarred) variables are defined as

$$(x, y) = (x^*, y^*)/B^*, \quad z = z^*/H^*, \quad h = h^*/H^*, \tag{A1}$$

$$\mathbf{u} = \frac{\rho K \mathbf{u}^*}{\tau_0 H^*}, \quad w = \frac{\rho B^* K w^*}{\tau_0 H^{*2}}, \tag{A2}$$

$$\eta = \frac{\rho g H^* \eta^*}{\tau_0 B^*}, \quad \text{and} \quad \tau_s = \tau^*/\tau_0, \tag{A3}$$

where B^* is the width of the continental shelf, H^* is the maximum depth, and τ_0 is the magnitude of the maximum wind stress. In terms of these variables, the linear, constant-density equations of motion take the nondimensional form

$$\nabla \cdot \mathbf{u} + w_z = 0 \quad \text{and}$$

$$\frac{\partial^2 \mathbf{u}}{\partial z^2} - \frac{2}{\delta_E^2}\mathbf{k} \times \mathbf{u} = \nabla \eta, \tag{A4}$$

where $\mathbf{k}$ is the unit vector in the vertical direction, ∇ is the horizontal gradient operator, and $\delta_E = (2K/fH^{*2})^{1/2}$. The ratio of the dimensional Ekman depth to the maximum depth, δ_E, is an index of the relative importance of friction to rotation. The boundary conditions are

$$\mathbf{u}_z = \tau_s, \quad w = 0, \quad \text{at} \quad z = 0 \quad \text{and}$$

$$\mathbf{u} = 0, \quad w = 0, \quad \text{at} \quad z = -h. \tag{A5}$$

Lateral mixing is ignored because the ratio $K_h H^{*2}/KB^{*2}$ (K_h represents the horizontal eddy viscosity, H^* is the maximum depth, and B^* is the shelf width) is assumed to be small. As a consequence, the only boundary condition imposed on the flow at the basin edges is that the normal velocity be zero or, equivalently, that the streamfunction be constant on those boundaries.

The solution of Eq. (A4) subject to Eq. (A5) is

$$\mathbf{u} = p_r \nabla \eta + p_i \mathbf{k} \times \nabla \eta + q_r \tau_s + q_i \mathbf{k} \times \tau_s, \tag{A6}$$

where

$$p = \frac{i\delta_E^2}{2}\left\{1 - \frac{\cos[(1-i)z/\delta_E]}{\cos[(1-i)h/\delta_E]}\right\}, \quad p_r = \mathrm{Re}(p), \quad p_i = \mathrm{Im}(p) \tag{A7}$$

and

$$q = \frac{i(1-i)\delta_E}{2}\frac{\sin[(1-i)(z+h)/\delta_E]}{\cos[(1-i)h/\delta_E]}, \quad q_r = \mathrm{Re}(q), \quad q_i = \mathrm{Im}(q). \tag{A8}$$

The velocity directly driven by the stress has two components, one parallel to and the other perpendicular to the wind, and the same is true for the velocity driven by the pressure gradient. Both p and q are functions of δ_E, z, and h.

The vertically integrated transport is

$$\mathbf{U} = \int_{-h}^{0} \mathbf{u}\, dz = P_r \nabla\eta + P_i \mathbf{k} \times \nabla\eta + Q_r \tau_s + Q_i \mathbf{k} \times \tau_s, \tag{A9}$$

where τ_s^x and τ_s^y are the components of the wind stress vector $\boldsymbol{\tau}_\mathbf{s}$, and P and Q are functions of h/δ_E:

$$P = \frac{i\delta_E^2}{2}\left\{h - \frac{\delta_E \tan[(1-i)h/\delta_E]}{1-i}\right\}, \quad P_r = \mathrm{Re}(P), \quad P_i = \mathrm{Im}(P) \tag{A10}$$

and

$$Q = \frac{i\delta_E^2}{2}\frac{1-\cos[(1-i)h/\delta_E]}{\cos[(1-i)h/\delta_E]}, \quad Q_r = \mathrm{Re}(Q), \quad Q_i = \mathrm{Im}(Q). \tag{A11}$$

Conservation of mass requires that $\nabla \cdot \mathbf{U} = 0$. This gives an equation for sea level:

$$P_r \nabla^2\eta + \nabla P_r \cdot \nabla\eta + \nabla\eta \times \nabla P_i = -\nabla \cdot (Q_r \boldsymbol{\tau}_s + Q_i \mathbf{k} \times \boldsymbol{\tau}_s); \tag{A12}$$

this is an elliptic partial differential equation that can be solved for η once the normal component of $\nabla\eta$ is specified on the boundaries.

Alternatively, introducing a transport streamfunction ψ defined as

$$\psi_x = \int_{-h}^{0} v\, dz, \quad \psi_y = -\int_{-h}^{0} u\, dz \tag{A13}$$

or

$$\mathbf{U} = \mathbf{k} \times \nabla\psi \tag{A14}$$

and noting that $\mathbf{k} \times \mathbf{k} \times \nabla\eta = -\nabla\eta$, the expression in Eq. (A9) for transport can be manipulated to give the following expression for the pressure gradient:

$$\nabla\eta = -A\mathbf{k} \times \nabla\psi - B\nabla\psi + C\boldsymbol{\tau}_s + D\mathbf{k} \times \boldsymbol{\tau}_s \tag{A15}$$

or, in component form,

$$\eta_x = A\psi_y - B\psi_x + C\tau_s^x - D\tau_s^y \quad \text{and} \tag{A16}$$

$$\eta_y = -A\psi_x - B\psi_y + C\tau_s^y + D\tau_s^x, \tag{A17}$$

where

$$A = -\frac{P_r}{P_r^2 + P_i^2}, \quad B = -\frac{P_i}{P_r^2 + P_i^2}, \tag{A18}$$

$$C = -\frac{Q_r P_r + Q_i P_i}{P_r^2 + P_i^2}, \quad \text{and} \quad D = \frac{Q_r P_i - Q_i P_r}{P_r^2 + P_i^2}. \tag{A19}$$

An equation for the streamfunction is obtained by taking the curl of Eq. (A15):

$$A\nabla^2\psi + \nabla A \cdot \nabla\psi + \nabla B \times \nabla\psi = C\nabla \times \boldsymbol{\tau}_s + \nabla C \times \boldsymbol{\tau}_s - \nabla \cdot D\boldsymbol{\tau}_s \tag{A20}$$

or

$$(A\psi_x)_x + (A\psi_y)_y + B_x\psi_y - B_y\psi_x = C[(\tau_s^y)_x - (\tau_s^x)_y] + C_x\tau_s^y - C_y\tau_s^x - (D\tau_s^x) - (D\tau_s^y)_y. \tag{A21}$$

Given appropriate boundary conditions, Eq. (A20) can be solved for ψ. The pressure gradient is then determined from Eq. (A15), the horizontal velocity is given by equation Eq. (A6), and the vertical velocity is evaluated by integrating the continuity equation down from the surface.

REFERENCES

Adams, J., 1989: MUDPACK: Multigrid FORTRAN software for the efficient solution of linear elliptic partial differential equations. *Appl. Math. Comput.,* **34,** 113–146.

Allen, J. S., and P. A. Newberger, 1996: Downwelling circulation on the Oregon continental shelf. Part I: Response to idealized forcing. *J. Phys. Oceanogr.,* **26,** 2011–2035.

——, ——, and J. Federiuk, 1995: Upwelling circulation on the Oregon continental shelf. Part I: Response to idealized forcing. *J. Phys. Oceanogr.,* **25,** 1843–1866.

Csanady, G. T., 1978: The arrested topographic wave. *J. Phys. Oceanogr.,* **8,** 47–62.

Gan, J., and J. S. Allen, 2002: A modeling study of shelf circulation off northern California in the region of the Coastal Ocean Dynamics Experiment: Response to relaxation of upwelling winds. *J. Geophys. Res.,* **107,** 3123, doi:10.1029/2000JC000768.

Huyer, A., and P. M. Kosro, 1987: Mesoscale surveys over the shelf and slope in the upwelling region near Point Arena, California. *J. Geophys. Res.,* **92,** 1655–1681.

Janowitz, G. S., and L. J. Pietrafessa, 1980: A model and observation of time-dependant upwelling over the mid-shelf and slope. *J. Phys. Oceanogr.,* **10,** 1574–1583.

Lopez, M., and A. J. Clarke, 1989: The wind-driven shelf and slope water flow in terms of a local and remote response. *J. Phys. Oceanogr.,* **19,** 1091–1101.

Pedlosky, J., 1974a: Longshore currents, upwelling and bottom topography. *J. Phys. Oceanogr.,* **4,** 214–226.

——, 1974b: On coastal jets and upwelling in bounded basins. *J. Phys. Oceanogr.,* **4,** 3–18.

Pringle, J. M., 2002: Enhancement of wind-driven upwelling and downwelling by alongshore bathymetric variability. *J. Phys. Oceanogr.,* **32,** 3101–3112.

Reid, J. L., G. L. Roden, and J. G. Wyllie, 1958: Studies of the California current system. California Cooperative Oceanic Fisheries Investigations, Progress Report, Scripps Institution

of Oceanography New Series No. 998, Marine Research Committee, California Department of Fish and Game, 27–56.

Stommel, H., 1948: The western intensification of wind-driven ocean currents. *Trans. Amer. Geophys. Union,* **29,** 202–206.

Sverdrup, H. U., M. W. Johnson, and R. H. Fleming, 1942: *The Oceans: Their Physics, Chemistry and General Biology.* Prentice Hall, 1087 pp.

Tilburg, C. E., 2003: Across-shelf transport on a continental shelf: Do across-shelf winds matter? *J. Phys. Oceanogr.,* **33,** 2675–2688.

Welander, P., 1976: A zonally uniform regime in the oceanic circulation. *J. Phys. Oceanogr.,* **6,** 121–124.

Winant, C. D., 2004: Three-dimensional wind-driven flow in an elongated, rotating basin. *J. Phys. Oceanogr.,* **34,** 462–476.

——, and C. E. Dorman, 1997: Seasonal patterns of surface wind stress and heat flux over the southern California bight. *J. Geophys. Res.,* **102,** 5641–5653.

——, ——, C. A. Friehe, and R. C. Beardsley, 1988: The marine layer off northern California: An example of supercritical channel flow. *J. Atmos. Sci.,* **45,** 3588–3605.